CZECH TECHNICAL UNIVERSITY IN PRAGUE
FACULTY OF NUCLEAR SCIENCES AND PHYSICAL ENGINEERING
DEPARTMENT OF PHYSICS

Programme: Mathematical Engineering
Branch of Study: Mathematical Physics

High pT jets in RunII of the ATLAS Experiment

MASTER'S DEGREE PROJECT

Author:	Jan Lochman
Supervisor:	Ing. Zdeněk Hubáček, Ph.D.
Submitted in:	May 2015

Zadani prace

Statement

Prohlasuji. . .

V Praze dne ....

Jan Lochman

Acknowledgment

Dekuji...

Jan Lochman

Název práce:
Jety s vysokou příčnou hybností v RunII experimentu ATLAS

Autor: Jan Lochman

Obor: Matematické Inženýrství

Druh práce: Diplomová práce

Vedoucí práce: Ing. Zdeněk Hubáček, Ph.D.
CERN

Abstrakt: Abstrakt CZ

Klíčová slova: Klicova slova

Title:
High pT jets in RunII of the ATLAS Experiment

Author: Jan Lochman

Abstract: Abstrakt EN

Key words: Key words

Contents

Introduction

Chapter 1

QCD

Is the purpose of theoretical physics to be no more than a cataloging of all the things that can happen when particles interact with each other and separate? Or is it to be an understanding at a deeper level in which there are things that are not directly observable (as the underlying quantized fields are) but in terms of which we shall have a more fundamental understanding?

Julian Schwinger

The theoretical framework of particle physics is called Standard Model (SM). The SM describes the way how the fundamental components of matter interact with each other through strong, weak and electromagnetic interactions. Mathematically the SM is gauge quantum field theory with local internal symmetries of the direct product group $SU(3) \times SU(2) \times U(1)$. Gauge bosons are assigned to generators of this symmetry - there are 8 massless gluons from $SU(3)$ and 3 massive $W^{\pm}, Z$ bosons with 1 massless boson γ from electroweak $SU(2) \times U(1)$ sector. Higgs mechanism has to be introduced in electroweak sector to assign $W^{\pm}, Z$ bosons mass and as consequence the new particle - Higgs boson - emerges in the SM theory. All bosons have integer spin.

In addition to the bosons the SM introduces spin1/2 fermions which are divided into three quark and three lepton families. Fermions are assumed to be point-like because there is no evidence for their internal structure to date. All fermions interact weakly, if they have electrical charge, they interact electromagnetically as well. Quarks are the only fundamental fermions which do interact strongly. System of fundamental particles of the SM is shown in figure 1.1.

Quarks bind together to form hadrons and there are hundreds (?source?) of known hadrons up to date. Hadrons are divided into baryons (3 quarks) and mesons (quark and anti-quark). Theory describing the interaction between quarks is called Quantum Chromodynamics (QCD) which key features will be discussed in this chapter. The reasoning for quark existence and for the description their strong interaction as $SU(3)$ gauge

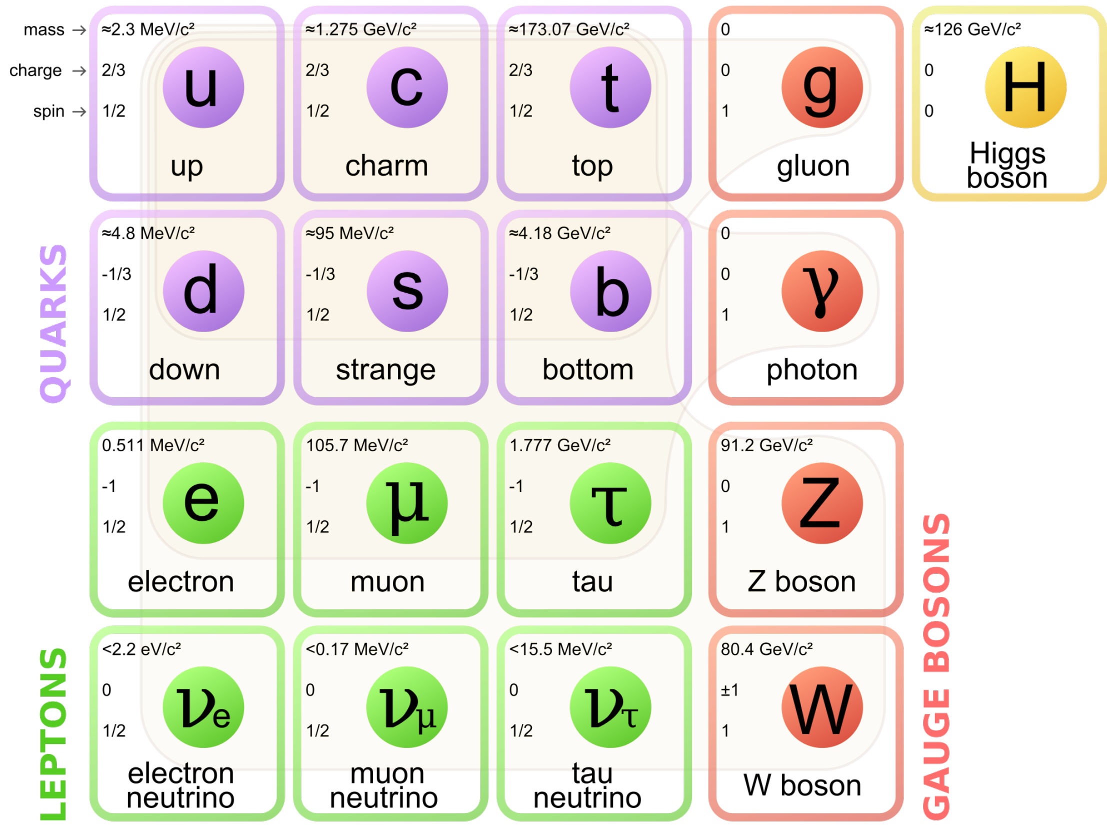

Figure 1.1: The system of fundamental particles of the SM. Figure from [1]

theory will be presented. Running coupling constant will be discussed to split QCD into perturbative and non-perturbative regions - two regions, where QCD has to use different mathematical approach for description of strong interaction. Most of ideas presented here is overtaken from the following textbook [2]. Electroweak sector of the SM is described in [3]. For more concise information about the SM the following textbooks can serve [4, 5].

1.1 Theoretical Ansatz

In 1950s there have already been discovered tens of new hadrons thanks to new particle accelerators and a lot of effort was exerted to categorize them. To each particle there was assigned a series of quantum numbers including isospin T with its third component T_3, hypercharge Y, electrical charge Q, strangeness S, baryon number B and others. Soon it was recognized, that there are some symmetries between these quantum numbers, like famous Gell-Mann–Nishijima relation [6, 7]

$$Q = T_3 + 1/2Y \quad , \quad Y = B + S + \dots , \tag{1.1}$$

	S	Y	T	T_3	Q
p	0	1	1/2	1/2	1
n				-1/2	0
Σ^+	-1	0	1	1	1
Σ^0				0	0
Σ^-				-1	-1
Λ			0	0	0
Ξ^0	-2	-1	1/2	1/2	0
Ξ^-				-1/2	-1

Table 1.1: Quantum numbers of selected baryons known in 1950s. S strangeness, Y hypercharge, T isospin, T_3 third component of isospin, Q electrical charge.

where dots denote charm, bottomness and topness and were introduced after work of Gell-Mann and Nishijima. Some of the baryons known by then are shown in table 1.1. In 1960s the known particles were successfully categorized with the so called Eightfold Way, which was published independently by Murray Gell-Mann [8] and George Zweig [9] in 1964. The Eightfold Way successfully predicted the existence of new particle Ω^- including its mass. Basic ideas of Eightfold way will be discussed in this section.

The key feature of Eightfold Way is to understand hadrons as the part of different representations of infinitesimal generators of $SU(3)$ flavor symmetry group. These infinitesimal generators of $SU(3)$ form the real eight-dimensional Lie algebra $\mathfrak{su}(3)$ which fundamental representation is usually derived from Gell-Mann matrices

$$\begin{aligned}
&\lambda_1 = \begin{pmatrix} 0 & 1 & 0 \\ 1 & 0 & 0 \\ 0 & 0 & 0 \end{pmatrix} \quad \lambda_2 = \begin{pmatrix} 0 & -i & 0 \\ i & 0 & 0 \\ 0 & 0 & 0 \end{pmatrix} \quad \lambda_3 = \begin{pmatrix} 1 & 0 & 0 \\ 0 & -1 & 0 \\ 0 & 0 & 0 \end{pmatrix} \\
&\lambda_4 = \begin{pmatrix} 0 & 0 & 1 \\ 0 & 0 & 0 \\ 1 & 0 & 0 \end{pmatrix} \quad \lambda_5 = \begin{pmatrix} 0 & 0 & -i \\ 0 & 0 & 0 \\ i & 0 & 0 \end{pmatrix} \\
&\lambda_6 = \begin{pmatrix} 0 & 0 & 0 \\ 0 & 0 & 1 \\ 0 & 1 & 0 \end{pmatrix} \quad \lambda_7 = \begin{pmatrix} 0 & 0 & 0 \\ 0 & 0 & -i \\ 0 & i & 0 \end{pmatrix} \quad \lambda_8 = \frac{1}{\sqrt{3}} \begin{pmatrix} 1 & 0 & 0 \\ 0 & 1 & 0 \\ 0 & 0 & -2 \end{pmatrix}.
\end{aligned} \tag{1.2}$$

The generators are usually chosen $g_a = \frac{1}{2}\lambda_a$ and obey the commutation relation $[g_a, g_b] = i f_{abc} g_c$ with f_{abc} being structure constants. Cartan subalgebra of fundamental representation of $\mathfrak{su}(3)$ is generated by $H_1 = g_3$ and $H_2 = g_8$. The eigenstates of three-dimensional representation of $\mathfrak{su}(3)$ can be chosen

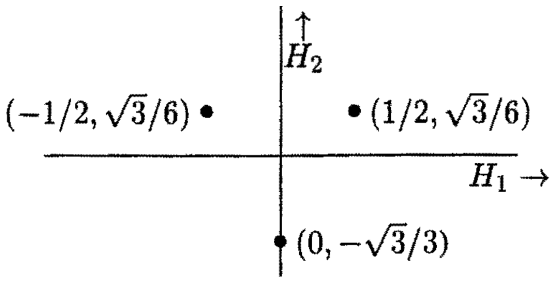

Figure 1.2: Eigenvalues of 3-dimensional representation of $\mathfrak{su}(3)$ Lie algebra. Figure from [10].

$$u = \begin{pmatrix} 1 \\ 0 \\ 0 \end{pmatrix} \leftrightarrow \left(\frac{1}{2}, \frac{\sqrt{3}}{6}\right), \quad d = \begin{pmatrix} 0 \\ 1 \\ 0 \end{pmatrix} \leftrightarrow \left(-\frac{1}{2}, \frac{\sqrt{3}}{6}\right), \quad s = \begin{pmatrix} 0 \\ 0 \\ 1 \end{pmatrix} \leftrightarrow \left(0, -\frac{\sqrt{3}}{3}\right), \tag{1.3}$$

where the eigenvalues to generators of the Cartan subalgebra was assigned $H_1 u = \frac{1}{2}u$, $H_2 u = \frac{\sqrt{3}}{6}u$ and similarly for d and s eigenstates. These eigenvalues are shown in figure 1.2. Other important representation of $\mathfrak{su}(3)$ is eight-dimensional adjoint representation. This representation has the following eigenstates and corresponding eigenvalues

$$\begin{aligned} \frac{1}{\sqrt{2}}(g_1 \pm ig_2) &\leftrightarrow (\pm 1, 0), \\ \frac{1}{\sqrt{2}}(g_4 \pm ig_5) &\leftrightarrow \left(\pm\frac{1}{2}, \pm\frac{\sqrt{3}}{2}\right), \\ \frac{1}{\sqrt{2}}(g_6 \pm ig_7) &\leftrightarrow \left(\mp\frac{1}{2}, \pm\frac{\sqrt{3}}{2}\right), \end{aligned} \tag{1.4}$$

where again when denoting $A = \frac{1}{\sqrt{2}}(g_1 + ig_2)$ then the upper sign of the first expression reads $[H_1, A] = A$ and $[H_2, A] = 0$ and similarly for remaining 5 eigenstates. Defining

$$H_1 = T_3 \quad \text{and} \quad H_2 = \frac{\sqrt{3}}{2}Y \tag{1.5}$$

one can easily assign hadrons from table 1.1 to corresponding eigenvalues of adjoint representation in (1.4) according to its third component of isospin T_3 and its hypercharge Y. This is depicted in figure 1.3.

When the same redefinition is done to the eigenstates of three-dimensional representation in (1.3), one can assign to eigenstates the hypercharge Y and strangeness S as well. The concrete values for states u, d, s are shown in table 1.2.

It is possible to find another representations of Lie algebra, to which the observed hadrons can be assigned. The simplest way seems to be through highest weight defining

<table>
<tr><th></th><th>S</th><th>Y</th><th>T</th><th>T_3</th><th>Q</th></tr>
<tr><td>u</td><td rowspan="2">0</td><td rowspan="2">1/3</td><td rowspan="2">1/2</td><td>1/2</td><td>2/3</td></tr>
<tr><td>d</td><td>-1/2</td><td rowspan="2">-1/3</td></tr>
<tr><td>s</td><td>-1</td><td>-2/3</td><td>0</td><td>0</td></tr>
</table>

Table 1.2: Quantum numbers of three quarks which existence was predicted by Gell-Mann and Zweig in 1964.

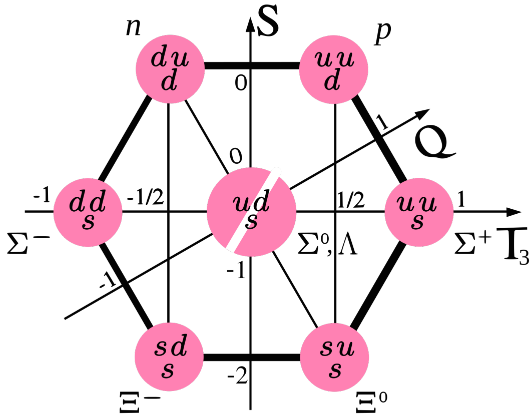

Figure 1.3: Baryonic octuplet encapsulating baryons from table 1.1. For baryons in this diagram, the relation $Y = S + 1$ holds. Figure from [11].

representation. From eigenvalues of adjoint representation (1.4) one can find simple roots $\alpha^1 = \left(\frac{1}{2}, \frac{\sqrt{3}}{2}\right)$, $\alpha^2 = \left(\frac{1}{2}, -\frac{\sqrt{3}}{2}\right)$, which are defining the highest weights $\mu^1 = \left(\frac{1}{2}, \frac{\sqrt{3}}{6}\right)$, $\mu^2 = \left(\frac{1}{2}, -\frac{\sqrt{3}}{6}\right)$. New representation of Lie algebra can be constructed from highest weight. This procedure is described in [10] in detail.

Representations defined by highest weight μ^1 or μ^2 respectively are called fundamental. Fundamental representation defined by μ^1 is usually denoted $\mathbf{3}$ and was encountered already by expressions (1.3) with weight diagram at figure 1.2, corresponding to three different quark states. The second fundamental representation corresponds to three anti-quark states and is usually denoted $\bar{\mathbf{3}}$. Representation depicted in figure 1.3 is defined by the highest weight $\mu^1 + \mu^2$.

Special interest is in representations with dimensions 10 and 8. These are present in decompositions $\mathbf{3} \otimes \mathbf{3} \otimes \mathbf{3} = \mathbf{10} \oplus \mathbf{8} \oplus \mathbf{8} \oplus \mathbf{1}$, which correspond to the baryons composed of three quarks, and $\mathbf{3} \otimes \bar{\mathbf{3}} = \mathbf{8} \oplus \mathbf{1}$ corresponding to mesons from quark and anti-quark.

Important feature of quark model just presented is its capability to predict hadron masses. This is done using Gell-Mann–Okubo mass formula [12, 13]

$$M = a_0 + a_1 S + a_2 \left(T(T+1) - \frac{1}{4} S^2 \right), \tag{1.6}$$

where a_0, a_1 and a_2 are free parameters which are common for all hadrons in one multiplet.

In 1970 Sheldon Lee Glashow, John Iliopoulos and Luciano Maiani proposed [14] an extension which predicted existence of fourth flavor of quark - charm quark. In 1973 the Makoto Kobayashi and Toshihide Moskawa proposed [15] that the existence of 6 different quark flavors could explain the experimental observation of CP violation.

1.2 Experimental Ground

In the previous section it was shown the hadrons can be categorized using representations of $\mathfrak{su}(3)$ Lie algebra. This lead to the model, where baryons were composed of three quarks whereas the mesons of quark and anti-quark. In this section, some experimental evidences will be presented to support quark model. First the scattering reactions will be discussed. It will be shown, that the lepton scattering on nucleons can be explained by assumption, that nucleons are composed of point-like spin-1/2 particles. Next discussion will address the fact, that there are three color charges - this will encounter the question, why the group $SU(3)$ is connected to the theory of strong interaction.

1.2.1 Scattering Reactions

One of the possibilities, how to find out, if there is some inner structure in nucleon N, are the scattering reactions

$$e^- \,(E \gg 1\,\mathrm{GeV}) + N \to e^- + N, \tag{1.7}$$

$$\nu_e \,(E \gg 1\,\mathrm{GeV}) + N \to \nu_e + N, \tag{1.8}$$

where the condition $E \gg 1\,\mathrm{GeV}$ is explicitly written to ensure the wavelength of lepton being $< 0.2\,\mathrm{fm}$. By the first scattering reaction, the information about electric charge distribution in nucleon can be extracted, whereas the second scattering reaction informs us about weak charge distribution. Further only (1.7) will be discussed. Feynmann diagram of this process is depicted with kinematics variables and vertex algebraic structures in figure 1.4.

Because of Lorentz-invariance of QED, the matrix element of the nucleon vertex $\bar{u}(P', S')\Gamma_\mu u(P, S)$ has to be Lorentz-vector. This restricts the possible form of Γ_μ to the following algebraic structure

$$\Gamma_\mu = A\gamma_\mu + BP'_\mu + CP_\mu + iDP'^\nu\sigma_{\mu\nu} + iEP^\nu\sigma_{\mu\nu}, \tag{1.9}$$

where A,...,E depend only on Lorentz-invariant quantities. Next condition which has to be taken into account, is gauge invariance of matrix element, which can be written in the form

$$q^\mu\bar{u}(P', S')\Gamma_\mu u(P, S). \tag{1.10}$$

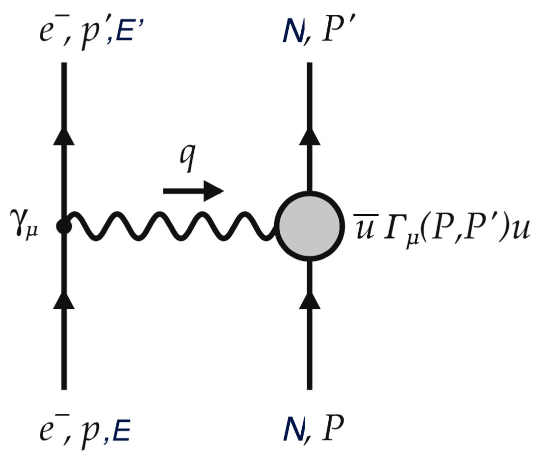

Figure 1.4: Scattering reaction $e^- N \to e^- N$. Figure from [2]

The further computation of cross section is straightforward and the result can be easily generalized to non-elastic scattering by which the nucleon in final state decays. The result is usually written using inelasticity parameter $y = \frac{E-E'}{E}$, $0 \leq y \leq 1$, $y = 0$ corresponding to the elastic scattering, Bjorken variable $x = \frac{Q^2}{2P\cdot q}$, $0 < x \leq 1$, $x = 1$ denoting elastic scattering and finally instead of negative value q^2 the $Q^2 = -q^2$ is used. Final result can be than written in the form

$$\left.\frac{d^2\sigma}{dxdy}\right|_{eN} = \frac{8\pi M_N E\alpha^2}{Q^4}\left[xy^2 F_1^{eN}(Q^2,x) + (1-y)F_2^{eN}(Q^2,x)\right]. \tag{1.11}$$

The eN sub(super)script stresses the fact, we are dealing with scattering (1.7). F_1^{eN} and F_2^{eN} are the so called structure functions, which are not determinable by the theory just presented - they have to be measured experimentally.

Structure constants were first measured by eP scattering at SLAC in 1968 [16] and shown the following results

1. for $Q^2 \geq 1\,\text{GeV}$, there is no significant dependence of structure functions on Q^2 and
2. for $Q^2 \geq 1\,\text{GeV}$, $F_2 \approx 2xF_1$.

These results can be explained by assumption nucleon being composed of point-like spin-1/2 constituents, for which R. P. Feynmann used term partons. In the following basic ideas of parton model will be presented. To ith parton, it is possible to assign momentum $P_{i,\xi}$

$$P_{i,\mu} = \xi_i P_\mu + \Delta P_{i,\mu} \quad , \quad \max_\mu(\Delta P_\mu) \ll \max_\mu P_\mu, \tag{1.12}$$

where $\xi_i \in \langle 0, 1\rangle$ and $\Delta P_{i,\mu}$ comes from the interaction between partons and it is assumed, the momentum coming from this interaction is much smaller than the total nucleon momentum P_μ. In addition, probabilities $f_i(\xi_i)$ that ith parton will carry ξ_i fraction of total momentum fulfilling

$$\int d\xi_i f_i(\xi_i) = 1 \tag{1.13}$$

must be defined. Then for scattering reaction (1.7) it can be derived the total cross section formula

$$\left.\frac{d^2\sigma}{dxdy}\right|_{eN} = \frac{4\pi M_N E\alpha^2}{Q^4}\left[y^2 + 2(1-y)\right]\sum_i f_i(x)q_i^2 x. \tag{1.14}$$

where for ith parton its electrical charge q_i was introduced. The last expression and (1.11) can be compared as polynomials in y resulting in

$$F_1^{eN}(x) = \frac{1}{2}\sum_i f_i(x)q_i^2 \quad , \quad F_2^{eN}(x) = \sum_i f_i(x)q_i^2 x. \tag{1.15}$$

It can be easily checked, that $F_2^{eN}(x) = 2xF_1^{eN}(x)$. Functions $f_i(x)$ just introduced are called Parton Distribution Functions (PDFs) and their important role in QCD will be discussed in (?somewhere?) in more details.

Important conclusion from analyzing of scattering reactions is, that the experimental results can be explained by assumption nucleons being composed of spin-1/2 point-like partons, now called quarks.

1.2.2 Number of Colors

Despite the strong confidence in parton model, theory which would describe the interaction between partons was still missing. There was no direct evidence on how the theory would look like at the beginning of 1970s. The theory of electroweak unification successfully suggested, that the gauge theories are the right theories for description of world at subatomic level, but to construct gauge theory of strong interaction the number of colors first had to be known.

Number of colors N_C is the number of different kinds of quarks of the same flavor with respect to the new interaction. In this part, three arguments will be presented to demonstrate, that $N_C = 3$.

The first argument is the analysis of the electron-positron anihilation into the pair of fermion and anti-fermion

$$e^+e^- \to f\bar{f}. \tag{1.16}$$

Feynmann diagram of this reaction is shown in figure 1.5, where constants sitting in two vertices are empahised. α stands for fine structure constants and Q_f for charge of fermion f in units of positron charge. Total cross section has to be proportional to

$$\sigma(e^-e^+ \to f\bar{f}) \sim Q_f^2\alpha^2. \tag{1.17}$$

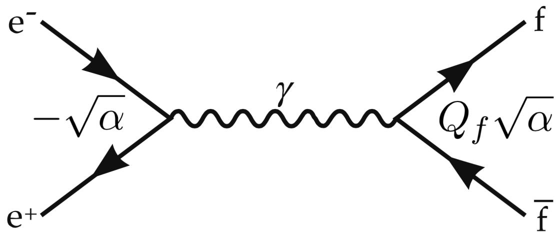

Figure 1.5: $e^+e^- \to f\bar{f}$ annihilation with vertex constants. α stands for fine structure constant, Q_f for charge of fermion f in units of positron charge.

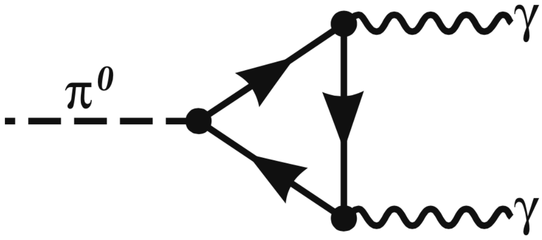

Figure 1.6: $\pi^0 \to 2\gamma$ decay with closed fermion loop.

In the case fermion f being quark, there is new degeneracy in final state coming from different colors of quarks in final state - the total cross section has to be multiplied by factor N_C. Experimentally, the so called R-factor is measured

$$R = \frac{\sigma(e^+e^- \to \text{hadrons})}{\sigma(e^+e^- \to \mu^+\mu^-)} = \left(\sum_q Q_q^2\right) N_C, \tag{1.18}$$

where sum on the left hand side is over all possible quark states. When the quark model proposed by Gell-Mann a Zweig is used, then for the quark charges in table 1.2

$$R = \left[\left(\frac{2}{3}\right)^2 + \left(\frac{-1}{3}\right)^2 + \left(\frac{-1}{3}\right)^2\right] N_C = \frac{2}{3} N_C. \tag{1.19}$$

Experimental results for R-ratio have shown (?citace?, ?concrete value?), that $N_C = 3$.

The second argument is the measurement of decay width of π_0 meson. Decay is depicted in figure 1.6. For decay width Γ it can be derived

$$\Gamma = 7.63 \left(\frac{N_C}{3}\right)^2 \text{eV}, \tag{1.20}$$

which, compared to the experimental value (?citace?, ?concrete value?) leads again to $N_C = 3$.

The third argument is purely theoretical and states, that the SM is internally consistent only if there are three colors (?citace?). This indicates that there is some linking between electroweak and strong sector of SM and motivates the search for Grand Unified Theories.

1.3 QCD as Gauge Theory

Putting arguments of previous section all together, there are strong experimental evidences, that nucleons consist of point-like spin-1/2 particles called quarks and that quarks bring into the theory new degeneracy factor $N_C = 3$, which can be understood as three different strong charges called colors.

Nowadays the quark-quark strong interaction is understood as an $SU(3)$ gauge theory in a degree of freedom called color. Gell-Mann matrices (1.2) can be chosen as generators of $SU(3)$. These matrices act on quark color triplets wave functions

$$\psi(x) = \begin{pmatrix} \psi_r(x) \\ \psi_g(x) \\ \psi_b(x) \end{pmatrix}. \tag{1.21}$$

Following the Yang-Mills theory [17], to each generator $\frac{\lambda^a}{2}$ gluon field $A^a_\mu(x)$ and gluon file strength tensor

$$F^a_{\mu\nu} = \left(\partial_\mu A^a_\nu - \partial_\nu A^a_\mu + g f^{abc} A^b_\mu A^c_\nu\right) \tag{1.22}$$

is assigned where g denotes the coupling constant of strong interaction and f^{abc} are structure constant defined in section 1.1. QCD Lagrangian

$$\mathscr{L}_{\mathrm{QCD}} = \bar{\psi}\left(-i\partial_\mu + g\frac{\lambda}{2}A^a_\mu(x)\right)\gamma^\mu\psi - \frac{1}{4}F^a_{\mu\nu}F^{\mu\nu}_a \tag{1.23}$$

is invariant under local transformation

$$\begin{aligned} \psi(x) &\to \psi'(x) = \mathrm{e}^{ig\Theta(x)}\psi(x), \\ A_\mu(x) &\to \mathrm{e}^{ig\Theta(x)}\left(A_\mu(x) + \frac{i}{g}\partial_\mu\right)\mathrm{e}^{-ig\Theta(x)}, \end{aligned} \tag{1.24}$$

where

$$\Theta(x) = \frac{1}{2}\lambda^a\Theta^a(x) \quad , \quad A_\mu(x) = \frac{1}{2}\lambda^a A^a_\mu(x). \tag{1.25}$$

There is no mass term in Lagrangian (1.23) because mass term $m\bar{\psi}\psi$ vary under gauge transformation (1.24). Origin of mass term lies in Higgs mechanism [18] which is explained in [3] in details.

QCD Lagrangian (1.23) together with gauge transformations (1.24) are sufficient for determination of Feynman rules - key ingredient in perturbative QCD which will be discussed in next section.

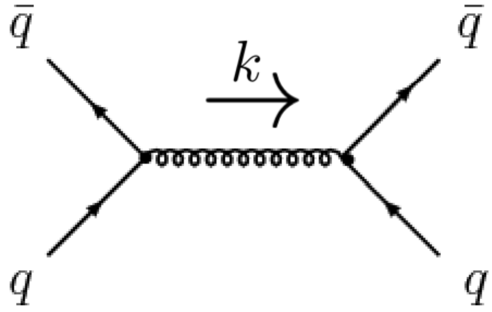

Figure 1.7: Leading order Feynmann diagrams in scattering reaction $q\bar{q} \to q\bar{q}$ with denoted transfered momentum k.

By derivation of gluon propagator, one has to add to the QCD Lagrangain the so called gauge-fixing term

$$\mathscr{L}_{\text{QCD}}^{\text{gauge-fixing}} = -\frac{1}{2\xi}\left(\partial_\mu A_a^\mu\right)^2, \tag{1.26}$$

which confines the possible gauges to one class parametrized by real parameter ξ. In non-Abelian gauge theories this term must be supplemented by the so called ghost term which brings into the theory new unphysical scalar particle obeying fermionic statistics. More details on so called Faddev-Popov ghost filed can be found in [19].

1.4 Perturbative QCD

Quantum Electrodynamics (QED) and QCD are both quantum filed gauge theories, but they differ in one killing feature - the former is Abelian whereas the latter is not. The non-Abelian character of QCD leads to new phenomenons which have the origin in QCD Lagrangian (1.23) directly leading to triple and quartic gluonic interactions. In this section one remarkable consequence will be discussed - the running coupling constant.

Assume scattering process

$$q\bar{q} \to q\bar{q}, \tag{1.27}$$

which is depicted in the lowest order of perturbation theory by the Feynman graph in figure 1.7. Except contribution of this graph to the scattering amplitude (which is the only contribution $\sim g^2$) there are 12 other Feynman diagrams with contributions $\sim g^4$. These are depicted in figure 1.8.

The contributions from new Feynman diagrams are calculated in [2] in detail. There is shown, that all this contributions together are logarithmically divergent. This divergence can be removed, when from the scattering amplitude for arbitrary momentum transfer k^2 scattering amplitude for fixed momentum transfer $k^2 = -M^2$ is subtracted. This is how the renormalized coupling constant g_R is obtained and here is its final expression

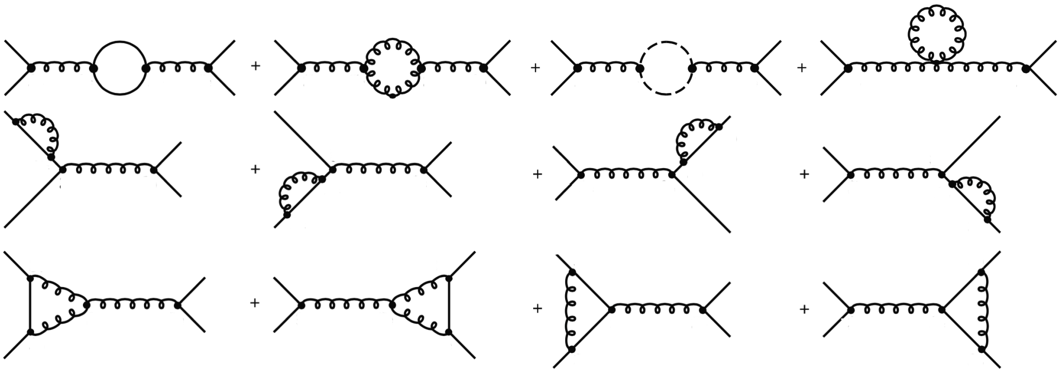

Figure 1.8: Next to the leading order Feynmann diagrams in scattering reactions $q\bar{q} \to q\bar{q}$. Dashed line represents scalar ghost particle.

$$g_R = g_0 - \frac{g_0^3}{16\pi^2}\left(\frac{11}{2} - \frac{1}{3}N_F\right)\ln\left(\frac{-k^2}{M^2}\right) + \mathscr{O}(g_0^5). \tag{1.28}$$

g_0 stands for the coupling constant measured at the renormalization scale $k^2 = -M^2$ and N_F is the number of different quark flavors with mass $m^2 \ll |k^2|$. Dependence of g_R on transfered momentum k^2 is evident, but there are another two intertwined dependences - on normalization scale M and on coupling constant at renormalization scale $g_0 = g_R|_{k^2=-M^2}$. For next purpose, it is convenient to use the dependence schema

$$g_R = g_R(-k^2, g_0(M)) \tag{1.29}$$

which allows the use of advantages of β-function and when the equation (1.28) is used, then the differential equation for $g_0(M)$ can be obtained

$$\beta(g_0) \equiv M\left(\frac{\partial g_R}{\partial M}\right)_{-k^2=M^2} = M\left(\frac{dg_0}{dM}\right)_{-k^2=M^2} \tag{1.30}$$

$$= -b_0 g_0^3 + \mathscr{O}(g_0^5), \quad b_0 = \frac{1}{16\pi^2}\left(11 - \frac{2N_F}{3}\right), \tag{1.31}$$

which can be solved directly to obtain coupling constant g_0 for arbitrary scale $-k^2$

$$\int_{g_0(M^2)}^{g_0(-k^2)} \frac{dg_0}{g_0^3} = -b_0 \int_{M^2}^{-k^2} \frac{dM}{M} \tag{1.32}$$

with solution

$$\alpha_S(-k^2) = \frac{\alpha_S(M^2)}{1 + \frac{\alpha_S(M^2)}{4\pi}\left(11 - \frac{2N_F}{3}\right)\ln\left(\frac{-k^2}{M^2}\right)}, \quad g_0^2(-k^2) = 4\pi\alpha_S(-k^2), \tag{1.33}$$

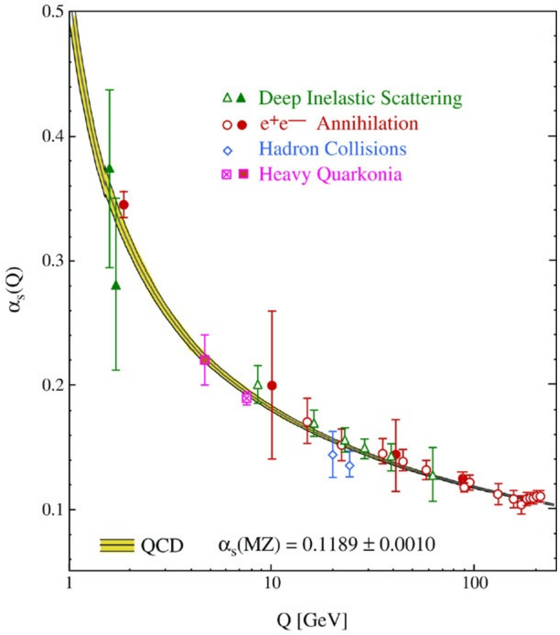

Figure 1.9: Experimental measurements of running coupling constant. $Q = \sqrt{|k^2|}$ in comparison to (1.33). (?source?) (?better picture?)

which is the final expression for running coupling constant up to one-loop order. This dependence corresponds to experimental data which are depicted in figure 1.9. Coupling constant decreases with increasing momentum transfer allowing the use of the perturbation theory. This is known as Asymptotic Freedom [20].

On the other hand, when the momentum transfer decreases, there is special value $-k^2 = \Lambda^2$ for which the last expression diverges

$$-1 = \frac{\alpha_S(M^2)}{4\pi}\left(11 - \frac{2N_F}{3}\right)\ln\left(\frac{\Lambda^2}{M^2}\right). \tag{1.34}$$

Experimental value is $\Lambda = 213^{+38}_{-35}\,\mathrm{MeV}$ [21] and demonstrates, that perturbative QCD cannot be used at low energy transfers. In fact, the running coupling constant $\alpha_S(-k^2)$ reaches value ~ 1 on momenta transfers $\sqrt{|k^2|} \sim 500\,\mathrm{MeV}$.

The behaviour of coupling constant at low energy transfers is not explainable in the language of perturpative QCD just presented. It is non-perturbative effect known as the principle of color confinment, which states, that quarks when seperate, the gluon force field between them becomes stronger and its energy is consumed by the creation of quark anti-quark pair. This continues until there is no free color charge left. This principle forbids us from observing free quarks.

To understand e.g. structure of proton with rest mass $< 1\,\mathrm{GeV}$ it is clear non-perturbative QCD has to be used. The ideas of non-perturbative QCD will be introduced in next section.

1.5 Non-Perturbative QCD

The most well established non-perturbative approach to QCD is the lattice QCD (LQCD). In this section basic features of the LQCD will be presented. More informations on this extended topic can be found in [2, 22].

LQCD is QCD formulated on a hypercubic equally spaced lattice in space and time with lattice parameter a denoting the distance between neighboring sites. Quark fields are placed on sites whereas the gluon fields sit on the links between neighboring sites. From QCD it inherits the gauge invariance which has to be formulated on lattice structure. For $a \to 0$ action of LQCD coincides with that of QCD. LQCD contains 6 parameters - strong coupling constant and masses of 5 quarks (the top quark with lifetime $\sim 10^{-24}\,\mathrm{s}$ is not assumed by the theory).

Unlike perturbative expansion used in continuous QCD, numerical evaluation of the path integral defining LQCD allows non-perturbative calculations. Practical LQCD calculations are limited by the availability of computational resources and the efficiency of algorithms. LQCD suffers with both statistical and systematic errors, the former arising from the use of Monte-Carlo integration, the latter, e.g. from the use of non-zero values of a.

Present LQCD calculations are made on supercomputers like the QCDCQ supercomputer [23] with peak speed of 500 TFlops using lattice spacing $a \sim 0.05 - 0.15\,\mathrm{fm}$ in lattice volume $V \sim (2 - 6\,\mathrm{fm})^3$.

The Importance of LQCD lies in its ability to predict mass spectrum of observed mesons and baryons, including quark masses itself, and in investigation of topological structure of QCD vacuum. LQCD can be used to obtain PDFs (1.13) helping us to understand the structure of hadrons. Phenomenology of LQCD explains also the principle of color confinment.

Chapter 2

QCD and The ATLAS Detector

2.1 Jet algorithms in ATLAS

Jet algorithm is a generic "recipe" which takes a set of particles (with defined four-momenta) and returns jets created from them. That recipe usually involves a set of parameters which together with the recipe fully specify the jet definition.

Principals of two jet algorithms are described here - fixed cone algorithm and k_t algorithm. First of these algorithms is more illustrative, the second one is used in ATLAS. Detailed description as well as other jet algorithms can be found in [24]. After definitions of jet algorithms it is shortly described, how the objects (not necessary particles) with defined four-momenta are constructed from the signal observed on the ATLAS detector.

2.1.1 Fixed cone algorithm

The first step of this algorithm is to order all input objects (reconstructed detector objects with four-momentum representation) in decreasing order in transverse momentum p_T. If the object with the highest p_T is above the seed threshold, all objects within a cone in pseudorapidity η and azimuth ϕ with $\Delta R = \sqrt{\Delta\eta^2 + \Delta\phi^2} < R_{cone}$, where R_{cone} is the fixed cone radius, are combined together. A new direction is calculated from the four-momenta inside the initial cone and a new cone is centered around it. Objects are then recollected in this new cone and again the direction is updated. This process continues until the direction of the cone does not change anymore after recombination, at which point the cone is considered stable and is called a jet. At this point, the next seed is taken from the input list and a new cone jet is formed with the same iterative procedure. This continues until no more seeds are available.

The jets found this way can share some constituents. This algorithm is not infrared safe. It means, that the presence of additional soft particles between two particles belonging to the same jet can affect the recombination of these two particles into a jet. In the same sense, the absence of additional soft particles between these two can disturb the correct reconstruction of the jet. This is ilustrated in Figure 2.1.

Parameters used by fixed cone algorithm are a seed threshold of $p_T > 1\,\mathrm{GeV}$, and a

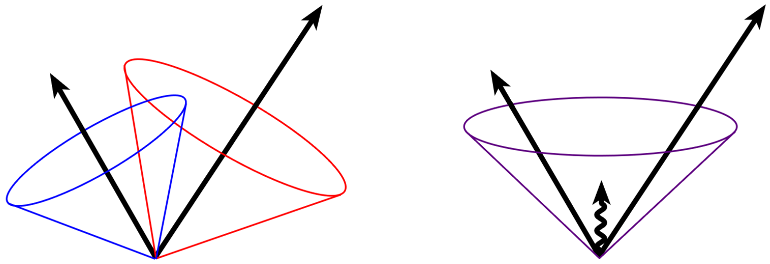

Figure 2.1: Fixed cone algorithm is not infrared safe - soft particle between two hard particles can determine, if hard particles end in different jets or will be part of the same one.

narrow ($R_{cone} = 0.4$) or a wide cone jet ($R_{cone} = 0.7$) option.

2.1.2 k_t algorithms

In this class of algorithms all pairs (i, j) of input objects are analyzed with respect to their relative transverse momentum squared, defined by

$$d_{ij} = \min\left(p_{T,i}^{2p}, p_{T,j}^{2p}\right)\frac{\Delta R_{ij}^2}{R^2} \tag{2.1}$$

and the squared p_T of object i relative to the beam axis

$$d_i = p_{T,i}^{2p}. \tag{2.2}$$

Here $\Delta R_{ij}^2 = (y_i - y_j)^2 + (\phi_i - \phi_j)^2$ and $p_{T,i}$, y_i and ϕ_i are respectively the transverse momentum, rapidity and azimuth of particle i. In addition to the radius parameter R, parameter p was added to split k_t algorithms into three categories.

- $p = 1$ k_t algorithm,
- $p = 0$ Cambridge/Aachen algorithm,
- $p = -1$ anti-k_t jet-clustering algorithm.

The differences between these algorithms are detailed described in [25].

These algorithms first find the minimum d_{min} of all d_{ij} and d_i. If d_{min} is in d_{ij}'s, the corresponding objects i and j are combined into a new object k using four-momentum recombination. Both objects i and j are removed from the list, and the new object k is added to it.

If d_{min} is in d_i's, the object i is considered to be a jet by itself and removed from the list.

This means that all original input objects end up to be either part of a jet or to be jets by themselves. Contrary to the cone algorithm described earlier, no objects are shared between jets and the procedure is infrared safe.

ATLAS uses anti-k_t algorithm with $R = 0.4$ for narrow and $R = 0.6$ for wide jets.

2.1.3 Calorimeter jets

The most important detectors for jet reconstruction are the ATLAS calorimeters. The ATLAS calorimeter system has about 200,000 individual cells of various sizes and with different readout technologies and cell geometries. For jet finding it is necessary to first combine these cell signals into larger signal object with physically meaningful four-momenta. The two concepts available are calorimeter signal towers and topological cell clusters.

In the case of calorimeter signal towers, the cells are projected onto a fixed grid in pseudorapidity η and azimuth ϕ. The tower bin size is $\Delta\eta \times \Delta\phi = 0.1 \times 0.1$ in the whole acceptance region of the calorimeters, i.e. in $|\eta| < 5$ and $-\pi < \phi < \pi$ with $100 \times 64 = 6,400$ towers in total.

The alternative representation of the calorimenter signals for jet reconstruction are topological cell clusters, which are basically an attempt to reconstruct three-dimensional "energy blobs" representing the showers developing for each particle entering the calorimeter. The clustering starts with seed cells with a signal-to-noise ratio, or signal significance $\Gamma = E_{cell}/\sigma_{noise,cell}$, above a certain threshold S, i.e. $|\Gamma| > S = 4$. All directly neighbouring cells of these seed cells, in all three dimensions, are collected into the cluster. Neighbours of neighbours are considered for those added cells which have Γ above a certain secondary threshold N ($|\Gamma| > N = 2$). Finally, a ring of guard cells with signal significances above a basic threshold $|\Gamma| > P = 0$ is added to the cluster. After the initial clusters are formed, they are analyzed for local signal maximums by a splitting algorithm, and split between those maximums.

2.2 The Large Hadron Collider and ATLAS Detector

2.2.1 The Large Hadron Collider

The Large Hadron Collider (LHC) [26, 27] is a charged particle accelerator located on the border of France and Switzerland, near Geneva. Built using the areas of the Large Electron-Positron collider, the main accelarator ring, of a 27 km circumference, is located around 100 m below the surface. There are four main experiments located around the ring: a large ion collider experiment (ALICE), a toroidal LHC apparatus (ATLAS), compact muon solenoid (CMS) and large hadron collider beauty (LHCb).

LHC started to operate on November 23, 2009 and soon thereafter (March 30, 2010) the proton-proton collisions achieved the center-of-mass energy $\sqrt{s} = 7\,\text{TeV}$, which is halve of the design energy of the machine. On April 5, 2012, the machine started its successful $\sqrt{s} = 8\,\text{TeV}$ run.

Next to the proton-proton collisions first heavy-ion Pb-Pb collisions took place in 2010 at a center of mass energy per pair of colliding nucleons $\sqrt{s} = 2.76\,\text{TeV}$. Proton-Pb collisions at $\sqrt{s} = 5.02\,\text{TeV}$ occurring on LHC during 3 weeks of 2013, successfully demonstrated LHC capability to provide asymmetric collisions.

The accelerator complex is currently being upgraded, and so are the LHC experiments. The machine will be back in 2015 with proton-proton collisions at $\sqrt{s} \sim 13\,\text{TeV}$.

Switching the beam crossing time from the current 50 ns to a 25 ns is still under consideration.

2.2.2 The ATLAS Detector

The ATLAS detector [28] is a general-purpose detector surrounding one of the interaction points of the LHC and with $\sim$ 100 million of individual electronic channels it is the most complicated instrument ever created having one simple task: Record charged particle collisions up to the center-of-mass energy per pair of colliding nucleons $\sqrt{s} = 14\,\text{TeV}$. A detector overview is shown in Figure 2.2a, where the main sub-detector systems can be seen: the inner detector, used to reconstruct charged-particle tracks, the electromagnetic calorimeters, the hadronic calorimeters, and the muon spectrometer.

ATLAS uses a right-handed coordinate system with its origin at the interaction point in the center of the detector and the z axis along the beam pipe. The x axis points from the interaction point to the center of the LHC ring, and the y axis points upward. Cylindrical coordinates (r, ϕ) are used in the transverse plane, ϕ being the azimuthal angle around the beam pipe. Instead of polar angle θ pseudorapidity η is used throughout this paper. For event selection the rapidity y plays an important role. In following definitions of pseudorapidity η and rapidity y, E stands for the total energy and p for size of total momentum:

$$\eta = -\frac{1}{2}\ln\left(\frac{p+p_z}{p-p_z}\right) = -\ln\left[\tan\left(\frac{\theta}{2}\right)\right], \tag{2.3}$$

$$y = -\frac{1}{2}\ln\left(\frac{E+p_z}{E-p_z}\right). \tag{2.4}$$

The transverse momentum p_T presents the component of momentum perpendicular to the beam line.

The main detector system relevant to this analysis is the ATLAS calorimeter, which is emphasized in Figure 2.2b. The calorimeter is divided into sub-detectors, providing overall coverage up to $|\eta| < 4.9$. The electromagnetic calorimeter, covering region $|\eta| < 3.2$, is a high-granularity sampling detector in which the active medium is liquid argon (LAr) interspaced with layers of lead absorber. The hadronic calorimeters are divided into three sections: a tile scintillator/steel calorimeter is used in both the barrel ($|\eta| < 1.0$) and extended barrel cylinders ($0.8 < |\eta| < 1.7$) while the hadronic endcap ($1.5 < |\eta| < 3.2$) consists of LAr/copper calorimeter modules. The forward calorimeter measures both electromagnetic and hadronic energy in the range $3.2 < |\eta| < 4.9$ using LAr/copper and LAr/tungsten modules.

Energy resolution of ATLAS calorimeter [**?**] is $\sim 15\,\%$ for jets with energies in the range $20\,\text{GeV} < E < 50\,\text{GeV}$ and decreases to $\sim 5\,\%$ for jets with energies $E > 1\,\text{TeV}$. Jet energy resolution is generally better in lower pseudorapidity regions.

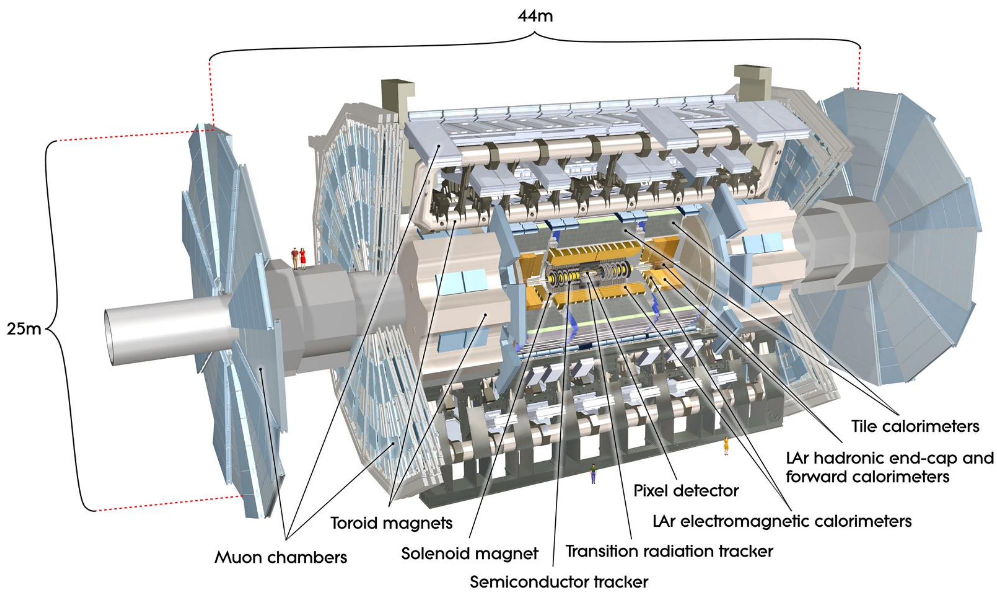

(a) ATLAS detector

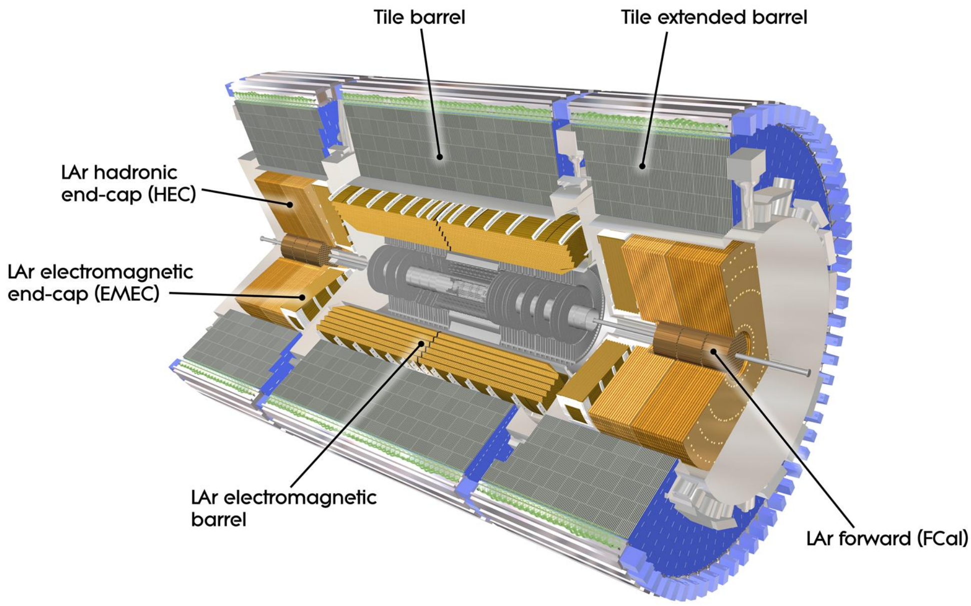

(b) Inner detector and calorimeter systems

Figure 2.2: (a) an overview of the ATLAS detector (b) detail on the inner detector and the calorimeters - the dominant sub-detector systems used in this paper. Figures from [29].

List of Figures

List of Tables

Bibliography

[1] "Standard model — Wikipedia, the free encyclopedia." http://en.wikipedia.org/wiki/Standard_Model, 2015.

[2] W. Greiner, D. Bromley, S. Schramm, and E. Stein, *Quantum Chromodynamics.* Springer, 2007.

[3] J. Horejsi, *Fundamentals of Electroweak Theory.* Karolinum Press, 2002.

[4] D. Griffiths, *Introduction to Elementary Particles.* Physics textbook, Wiley, 2008.

[5] W. Cottingham and D. Greenwood, *An Introduction to the Standard Model of Particle Physics.* Cambridge University Press, 2007.

[6] T. Nakano and K. Nishijima, "Charge independence for v-particles," *Progress of Theoretical Physics*, vol. 10, no. 5, pp. 581–582, 1953.

[7] M. Gell-Mann, "The interpretation of the new particles as displaced charge multiplets," *Il Nuovo Cimento*, vol. 4, no. 2, pp. 848–866, 1956.

[8] M. Gell-Mann and Y. Ne'eman, *The eightfold way.* Frontiers in Physics, New York, NY: Benjamin, 1964.

[9] G. Zweig, "An SU_3 model for strong interaction symmetry and its breaking; Version 2," p. 80 p, Feb 1964.

[10] H. Georgi, *Lie Algebras in Particle Physics: From Isospin to Unified Theories.* Frontiers in Physics Series, Westview Press, 1999.

[11] "Eightfold way — Wikipedia, the free encyclopedia." http://de.wikipedia.org/wiki/Eightfold_Way, 2015.

[12] M. Gell-Mann and H. Fritzsch, *Murray Gell-Mann: selected papers.* World Scientific series in 20th century physics, Singapore: World Scientific, 2010.

[13] S. Okubo, "Note on unitary symmetry in strong interactions," *Progress of Theoretical Physics*, vol. 27, no. 5, pp. 949–966, 1962.

[14] S. L. Glashow, J. Iliopoulos, and L. Maiani, "Weak interactions with lepton-hadron symmetry," *Phys. Rev. D*, vol. 2, pp. 1285–1292, Oct 1970.

[15] M. Kobayashi and T. Maskawa, "Cp-violation in the renormalizable theory of weak interaction," *Progress of Theoretical Physics*, vol. 49, no. 2, pp. 652–657, 1973.

[16] E. D. Bloom, D. H. Coward, H. DeStaebler, J. Drees, G. Miller, L. W. Mo, R. E. Taylor, M. Breidenbach, J. I. Friedman, G. C. Hartmann, and H. W. Kendall, "High-energy inelastic $e-p$ scattering at 6° and 10°," *Phys. Rev. Lett.*, vol. 23, pp. 930–934, Oct 1969.

[17] C. N. Yang and R. L. Mills, "Conservation of isotopic spin and isotopic gauge invariance," *Phys. Rev.*, vol. 96, pp. 191–195, 1954.

[18] P. W. Higgs, "Broken symmetries and the masses of gauge bosons," *Phys. Rev. Lett.*, vol. 13, pp. 508–509, Oct 1964.

[19] L. Faddeev and V. Popov, "Feynman diagrams for the yang-mills field," *Physics Letters B*, vol. 25, no. 1, pp. 29 – 30, 1967.

[20] D. J. Gross and F. Wilczek, "Ultraviolet behavior of non-abelian gauge theories," *Phys. Rev. Lett.*, vol. 30, pp. 1343–1346, Jun 1973.

[21] "The history of qcd — cern courier." `http://cerncourier.com/cws/article/cern/50796`, 2015.

[22] R. Gupta, "Introduction to lattice QCD: Course," pp. 83–219, 1997.

[23] A. Ukawa, "Kenneth Wilson and lattice QCD," 2015.

[24] G. Aad *et al.*, "Expected Performance of the ATLAS Experiment - Detector, Trigger and Physics," 2009.

[25] M. Cacciari, G. P. Salam, and G. Soyez, "The Anti-k(t) jet clustering algorithm," *JHEP*, vol. 0804, p. 063, 2008.

[26] L. Evans and P. Bryant, "Lhc machine," *Journal of Instrumentation*, vol. 3, no. 08, p. S08001, 2008.

[27] G. Landsberg, "LHC: Past, Present, and Future," 2013.

[28] T. A. Collaboration, "The atlas experiment at the cern large hadron collider," *Journal of Instrumentation*, vol. 3, no. 08, p. S08003, 2008.

[29] *Expected performance of the ATLAS experiment: detector, trigger and physics.* Geneva: CERN, 2009.